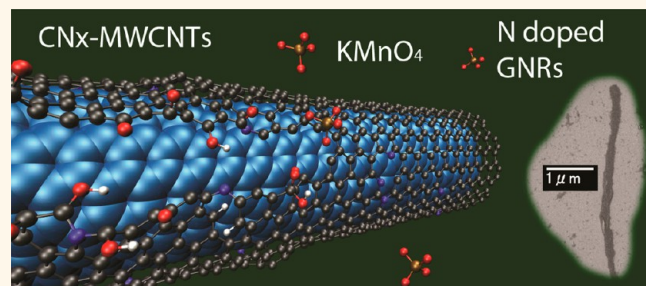


Formation of Nitrogen-Doped Graphene Nanoribbons *via* Chemical Unzipping

Rodolfo Cruz-Silva,[†] Aaron Morelos-Gómez,[§] Sofía Vega-Díaz,[†] Ferdinando Tristán-López,[†] Ana L. Elias,[‡] Nestor Perea-López,[‡] Hiroyuki Muramatsu,[§] Takuya Hayashi,[†] Kazunori Fujisawa,[†] Yoong Ahm Kim,[†] Morinobu Endo,[†] and Mauricio Terrones^{†,‡,*}

[†]Research Center for Exotic Nanocarbons, Shinshu University, 4-17-1 Wakasato, Nagano 380-8553, Japan, [‡]Department of Physics, Department of Materials Science and Engineering & Center for 2-Dimensional and Layered Materials, The Pennsylvania State University, University Park, Pennsylvania 16802, United States, and [§]Faculty of Engineering, Shinshu University, 4-17-1 Wakasato, Nagano 380-8553, Japan

ABSTRACT In this work, we carried out chemical oxidation studies of nitrogen-doped multiwalled carbon nanotubes (CNx-MWCNTs) using potassium permanganate in order to obtain nitrogen-doped graphene nanoribbons. Reaction parameters such as oxidation reaction, reaction time, the oxidizer to nanotube mass ratio, and the temperature were varied, and their effect was carefully analyzed. The presence of nitrogen atoms makes CNx-MWCNTs more reactive toward oxidation when compared to undoped multiwalled carbon nanotubes (MWCNTs). High-resolution transmission electron microscopy studies indicate that the oxidation of the graphitic layers within CNx-MWCNTs results in the unzipping of large diameter nanotubes and the formation of a disordered oxidized carbon coating on small diameter nanotubes. The nitrogen content within unzipped CNx-MWCNTs decreased as a function of the oxidation time, temperature, and oxidizer concentration. By controlling the degree of oxidation, the N atomic % could be reduced from 1.56% in pristine CNx-MWCNTs down to 0.31 atom % in nitrogen-doped oxidized graphene nanoribbons. A comparative thermogravimetric analysis reveals a lower thermal stability of the (unzipped) oxidized CNx-MWCNTs when compared to MWCNT samples. The oxidized graphene nanoribbons were chemically and thermally reduced and yielded nitrogen-doped graphene nanoribbons (N-GNRs). The thermal reduction at relatively low temperature (300 °C) results in graphene nanoribbons with 0.37 atom % of nitrogen. This method represents a novel route to preparation of bulk quantities of nitrogen-doped unzipped carbon nanotubes, which is able to control the doping level in the resulting reduced GNR samples. Finally, the electrochemical properties of these materials were evaluated.



KEYWORDS: nanotube unzipping · nitrogen doping · graphene nanoribbons · carbon nanotubes

Soon after reporting the isolation of graphene and the discovery of its outstanding properties,¹ a great deal of attention was paid to two-dimensional nanocarbons. Strips of graphene sheets, also known as graphene nanoribbons (GNRs), are one-dimensional graphene-based materials exhibiting different physicochemical properties when compared to carbon nanotubes. Since the pioneering work of Fujita *et al.*,² it is well-known that the edge configuration, either on zigzag or armchair, plays a fundamental role in the electronic properties of GNRs. The edges are highly reactive, and if GNRs are narrow (*e.g.*, <10 nm wide), they could behave as semiconducting

or metallic one-dimensional wires depending on their edge termination.³ The fact that graphene is one of the strongest materials ever known makes GNRs very attractive as reinforcement in the fabrication of nanocomposites. In addition, due to the good mechanical properties of graphene, GNRs combine a high aspect ratio that facilitates their blending with polymers in the molten state and the possibility to functionalize their edges to improve their compatibility with polymer matrices.⁴ When compared to carbon nanotubes, in which their outer surface is mainly a basal graphitic plane, GNRs possess reactive edges and might even exhibit step-edges that could enhance the

* Address correspondence to mut11@psu.edu, mtterrones@shinshu-u.ac.jp.

Received for review November 6, 2012 and accepted February 19, 2013.

Published online February 19, 2013
10.1021/nn305179b

© 2013 American Chemical Society

adsorption⁵ and electrocatalysis⁶ of certain molecules on their surfaces. Among the methods used so far to prepare graphene nanoribbons, there are bottom-up approaches such as chemical vapor deposition (CVD)⁷ and chemical synthesis,⁸ but top-down methods have also been reported.⁹ These top-down methods are mainly based on the unzipping of carbon nanotubes by different techniques such as plasma cutting,¹⁰ catalytic cutting,¹¹ intercalation–exfoliation,^{12,13} electrical¹⁴ and electrochemical unzipping,¹⁵ and chemical oxidation/reduction.^{16–19} Among these methods, the latter appears to be a straightforward technique which could be used to easily produce bulk amounts of GNRs, from grams to even tons; however, due to the partially irreversible oxidation, the residual defective sites will result in ribbons with inferior electrical conductivity and electron mobility as compared to highly crystalline ribbons prepared by other routes. In addition, the chemical oxidation/reduction method is relatively simple, and in this way, single- and few-layer GNRs have been synthesized and their physicochemical properties reported.

While the properties of GNRs strongly depend on their geometric parameters (thickness, width, length, and edge termination), chemical and structural modifications of the nanoribbons can also drastically modify their performance. Indeed, one way to modify the electronic and chemical properties of GNRs is by doping, and only a few papers have been published in this respect.^{3,20–22} The presence of defects,^{23,24} functional groups,²⁵ and heteroatoms such as boron^{26,27} and nitrogen,^{28,29} among other features,²² could also modify the properties of GNRs. Nitrogen-doped GNRs (N-GNRs) are particularly interesting because nitrogen atoms could be used extensively to modify grapheme-like nanostructures, such as graphene or carbon nanotubes. N-GNRs have been studied, and theoretical calculations suggest that nitrogen atoms located at their edges and near the edges might promote the electrocatalytic activity of GNRs toward the oxygen reduction reaction.³⁰ Doping could also be used to modify the energy gap of GNRs and tune their electronic properties.^{29,31–33} In spite of the huge potential of N-GNRs and the amount of theoretical reports on the subject, there are only very few experimental reports dealing with the synthesis and characterization of N-GNRs. Elias *et al.*¹¹ used metal nanoparticles as catalytic nanoscissors to longitudinally unzip MWCNTs and CNx-MWCNTs, obtaining a mixture of graphene-like sheets, including N-GNRs, and partially unzipped nanotubes. While it is well-known that the nitrogen atoms increase the reactivity of MWCNTs, the role of these defects upon strong oxidation/exfoliation/reduction has not been reported hitherto. Recently, Wei *et al.*²⁰ carried out the chemical oxidation of CNx-MWCNTs. It was found that some nanotubes were shortened and split into nanoribbons, but it was concluded that in

most nanotubes the tubular structure was preserved after the oxidation, even though the outer surface was highly oxidized. In this work, we report the synthesis of N-GNRs by a wet chemical oxidation process, starting from CNx-MWCNTs, followed by their thermal (and/or chemical) reduction. For different synthesis conditions, we studied the effect of the reaction time, oxidizer concentration and temperature, and analyzed the products by X-ray photoemission spectroscopy (XPS), scanning electron microscopy (SEM), and transmission electron microscopy (TEM). In our case, the unzipping of CNx-MWCNTs was successful and we obtained oxidized N-GNRs (ox-N-GNRs). These oxidized ribbons were then reduced *via* chemical and thermal reduction processes in order to synthesize crystalline N-GNRs. To the best of our knowledge, this appears to be the first work describing the oxidation/reduction mechanisms associated with the production of N-GNRs.

RESULTS AND DISCUSSION

The unzipping of pure MWCNTs using potassium permanganate has already been optimized^{16,17} by Tour's group; however, the reactivity of CNx-MWCNTs is very different from pure carbon nanotubes, and thus, we used slight modifications of the reaction parameters in order to optimize the unzipping of CNx-MWCNTs. Table 1 summarizes the results related to the obtained morphologies (using SEM) and the oxidation degree (calculated from XPS) after the oxidation reactions. The CNx-MWCNTs used in this study are large diameter nanotubes with relatively low nitrogen content (1.55–1.7 nitrogen atom % as determined by XPS). SEM image, diameter distribution, TEM image, XPS spectrum, and TGA analysis of pristine CNx-MWCNTs can be found in the Supporting Information (Figure S1). In reactions 1–4, the KMnO₄ to CNx-MWCNTs mass ratio was fixed to 5 and the oxidation temperature was varied from 20 to 80 °C. In order to study the amount of oxidizer, we carried out reactions 5 and 6, in which the reaction temperature was set to 60 °C and the KMnO₄ to CNx-MWCNTs mass ratio was changed to 1 and 2.5. We compared the oxidation of CNx-MWCNTs with other types of carbon materials such as pristine MWCNTs produced in our laboratory using CVD (Run 7), highly crystalline MWCNTs (Run 8), and graphite (Run 9). Reactions 1–4 reveal that the oxidation strength of permanganate solutions is strongly dependent on the temperature, and the C/O ratio varied from 3.31 to 2.16 as the temperature increased from 20 to 80 °C. The C/O ratios in our work are consistently higher than those reported by Higginbotham *et al.*¹⁶ This difference might be due to experimental differences (XPS sensitivity factors, reactor design, purification procedure, etc). The oxidation extent, as measured from the C/O ratio, did not increase with temperatures over 60 °C (reaction 4), as reported for MWCNTs,¹⁶ but the reaction

TABLE 1. Summary of Oxidation Conditions and Results

Run	Type of material	Temp KMnO ₄	SEM	XPS data				Observations
				Peak	Position	at. %	C/O	
1	ox-N-GNRs	20°C 5x		O 1s	532.6	22.9		Stacked ribbons with different shapes (helicoidal, flat, and u shaped). Light oxidation.
2	ox-N-GNRs	40°C 5x		O 1s	532.9	29.73		Stacked ribbons with different shapes (flat and u shaped). Moderate oxidation
3	ox-N-GNRs	60°C 5x		O 1s	532.6	32.19		Mainly stacked ribbons with few exfoliated ribbons. High oxidation
4	ox-N-GNRs	80°C 5x		O 1s	532.7	31.5		Mixture of exfoliated and stacked ribbons. High oxidation
5	ox-N-GNRs	60°C 1x		O 1s	532.5	22.32		Stacked ribbons with u shape. Light oxidation
6	ox-N-GNRs	60°C 2.5x		O 1s	532.7	28.29		Mainly stacked ribbons. Moderate oxidation.
7	ox-GNRs	80°C 5x		C 1s	286.7	75.23		Mainly exfoliated ribbons. Moderate oxidation.
8	ox-HC-GNRs	80°C 5x		O 1s	530.2	24.08	3.12	Mainly exfoliated ribbons assemble as sheets. Moderate oxidation.
9	Graphite oxide (GO)	40°C 5x		C 1s	286.6	69.89		Fully exfoliated GO sheets. High Oxidation

prepared at 80 °C resulted in oxidized N-doped GNRs that could be exfoliated by a slight ultrasound treatment that resulted in ultrathin nanoribbons. High-resolution SEM images of the different types of oxidized N-GNRs are shown in Figure 1. The unzipping of nanotubes led to four basic types of nanoribbons represented in Figure 1a–d, and they could be described according to its shape as longitudinally unzipped

nanotubes (Figure 1a), helicoidally unzipped nanotubes (Figure 1b), “stiff” nanoribbons (Figure 1c), and “soft” nanoribbons (Figure 1d). Nanoribbons exhibiting morphologies shown in (b) and (c) are the result of a mild oxidation (termed “stiff” nanoribbons because they can form free-standing nanostructures) and were obtained only in reactions 1, 2, 5, and 6. On the other hand, “soft” nanoribbons (Figure 1d) are the result of an

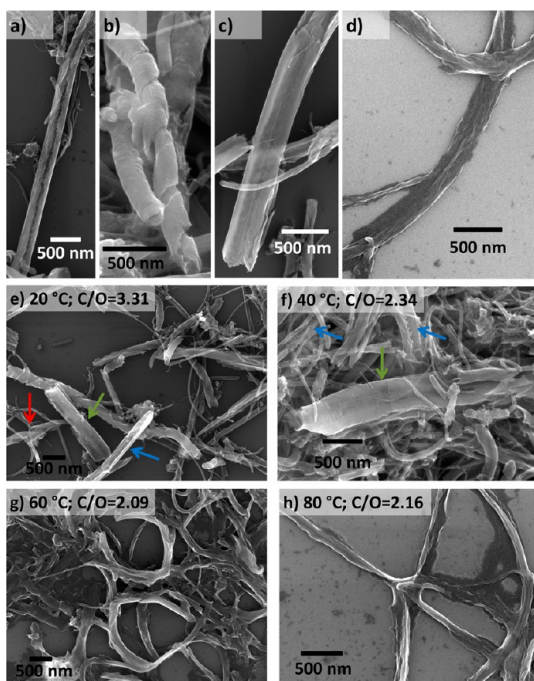


Figure 1. SEM images depicting the morphologies of the oxidized N-doped graphene nanoribbons (ox-N-GNRs). (a) Longitudinally unzipped nanotube, (b) helically unzipped nanotubes, (c) “stiff” N-doped oxidized graphene nanoribbon (with flat shape), and (d) “soft” N-doped oxidized graphene nanoribbon (highly oxidized). Representative images of the oxidized N-doped nanoribbons prepared at different temperatures are also shown: (e) 20 °C, (f) 40 °C, (g) 60 °C, and (h) 80 °C.

almost complete oxidation of the sp^2 graphitic network that resulted in a sp^3 -like lattice with enhanced chemical activity. These “soft” nanoribbons are not free-standing structures; instead, the nanoribbons adhere completely to the substrate upon drying.

High-resolution images of nanotube samples unzipped at 20 and 40 °C (Figure 1e,f, respectively) confirm the presence of large diameter nanotubes that could be easily oxidized and unzipped into ribbons of about 150–400 nm in width; note that very small diameter nanotubes (<30 nm) did not unzip. “Soft” nanoribbons were not observed under these conditions. After longitudinal unzipping, the inner features of the bamboo-like structure of CNx-MWCNTs were preserved (Figure 1e,f, blue arrows). Some of these CNx-MWCNTs unzipped, resulting in twisted nanoribbons, suggesting that the tube chirality might influence the unzipping process (Figure 1b,e, red arrow). The morphology of nanoribbons, such as those shown in Figure 1a, indicates that light oxidation with $KMnO_4$ results in nanotube unzipping without exfoliation of the nanotube walls. However, when high oxidation took place, structural changes occurred at 60 °C (Figure 1g), thus resulting in shortened and curled unzipped nanotubes and some exfoliated material. Structures such as those shown in Figure 1a–c were not found at 60 or 80 °C. During centrifugation of the samples oxidized at 60 and 80 °C, dark supernatants were observed,

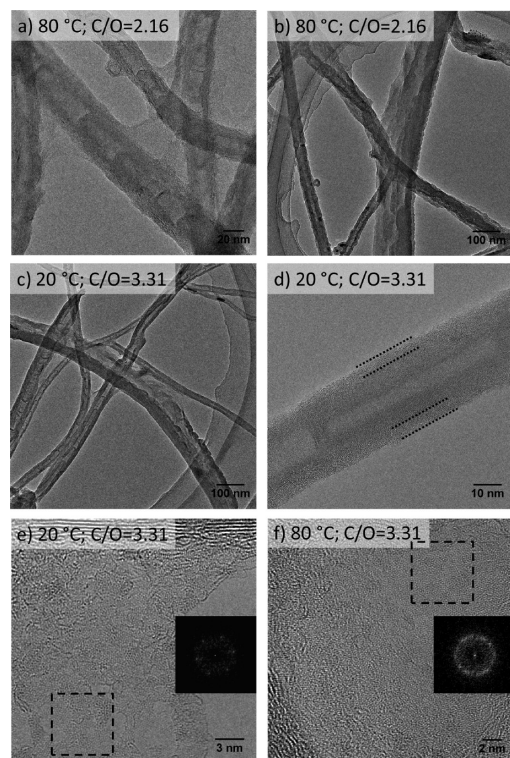


Figure 2. HRTEM images of oxidized N-doped graphene nanoribbons (ox-N-GNRs). (a,b) Two magnifications of the sample highly oxidized ($C/O = 2.16$) prepared at 80 °C. (c,d) Two magnifications of the sample mildly oxidized ($C/O = 3.31$) prepared at 20 °C. The formation of an amorphous-like coating can be observed on the structures regardless of the temperature. Exfoliated N-doped few-layer graphene sheets exfoliated from nanotubes at different temperatures are observed at (e) 20 °C and (f) 80 °C.

possibly due to the presence of very small fragments of water-dispersible carbonaceous flakes, suggesting the successful exfoliation of the ox-N-GNRs.

In order to study if the oxidation extent could be controlled by limiting the amount of oxidizer, ox-N-GNRs were prepared at 60 °C using 1:1 and 2.5:1 oxidizer to nanotube mass ratio, instead of using the typical 5:1 ratio (see Supporting Information Figure S2a,b, respectively). These experiments resulted in “stiff” ribbon structures with morphologies very similar to those obtained at 40 and 20 °C, respectively (Figure 1f,e). These results clearly indicate that the oxidation extent determines the morphology of the unzipped nanotubes. In this context, we propose the following morphology evolution of the nanotubes, as the oxidation degree increases: (1) pristine CNx material, (2) mildly oxidized unzipped structures (similar to those shown in Figure 1a,b), (3) flat-shaped nanoribbons (see Figure 1c), and finally, (4) “soft” nanoribbons such as those shown in Figure 1d,h. We also noted that some nanoribbons exhibit a curled (or helicoidally shaped) morphology, such as that shown in Figure 1g. These curled geometries appear as a result of the oxidation, which starts from the open ends and, after unzipping, continues from the edges advancing toward the middle of the

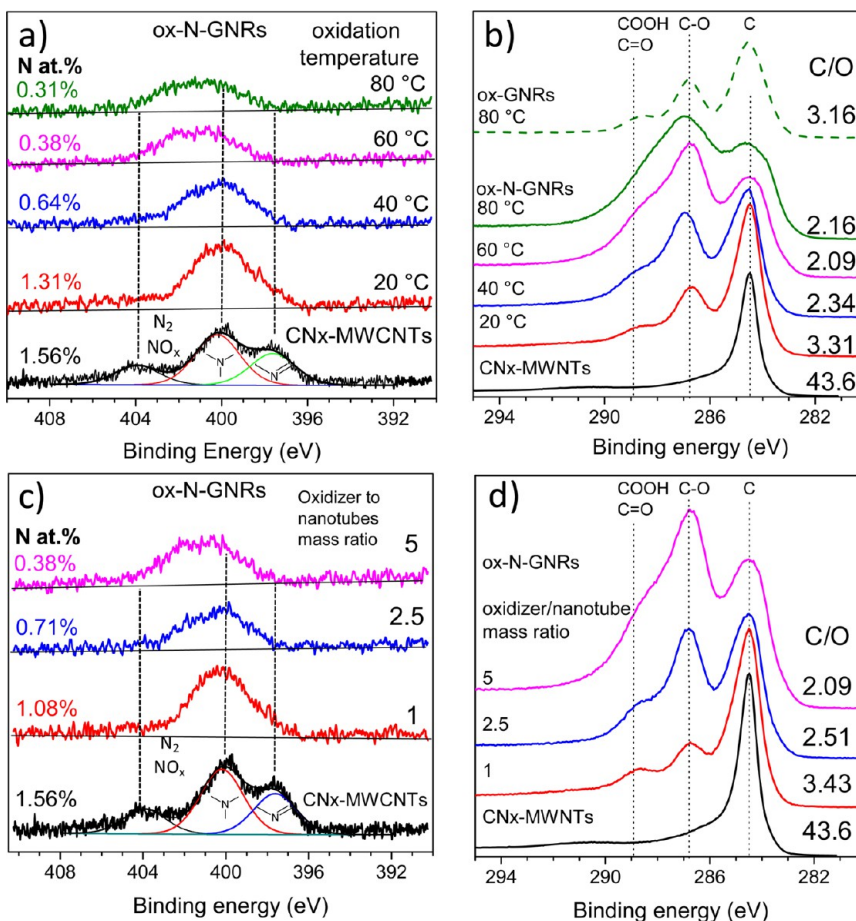


Figure 3. C 1s and N 1s X-ray photoelectron spectra of ox-N-GNRs. (a) N 1s core-level spectra and (b) C 1s core-level spectra of the ox-N-GNRs prepared using a fixed 5:1 oxidizer to CNx-MWCNTs mass ratio showing the effect of the oxidation temperature. Similarly, oxidation reactions performed at the same temperature with different amount of oxidizer display different oxidation degree as witnessed in (c) N 1s core-level spectra and (d) C 1s core-level spectra of samples prepared at 60 °C with different oxidizer to CNx-MWCNTs ratio. The duration of oxidation time for all materials was 2 h.

unzipping nanotube, similar to the mechanism reported for graphite flakes by Pan and Aksay.³⁴ We believe oxidation in anisotropic expansion results in curling of the nanoribbon when partially oxidized.

The morphology of the N-GNRs was also studied by HRTEM. Figure 2a,b shows a low-magnification image of the ox-N-GNR sample prepared at 80 °C. The oxidized nanotubes shown in Figure 2a with diameters of less than 50 nm were not unzipped and still retain the bamboo-like compartments, characteristic of CNx-MWCNTs. However, they appear coated with a layer of amorphous-like material of *ca.* 5–10 nm thick. Figure 2b shows a nanoribbon of 160 nm width and variable thickness as well as a partially unzipped nanotube. Figure 2c shows the material prepared at 20 °C displaying a bent nanotube which was fully unzipped (similar to the structure shown in Figure 1a). In this image, small diameter nanotubes that were not unzipped could also be observed. Figure 2d shows a HRTEM image of one of these not unzipped nanotubes in which a 6 nm thick amorphous coating (see dotted lines) is observed on its surface. During oxidation, single-layer or few-layer graphene was exfoliated from the nanotubes.

Figure 2e shows a layer attached to a nanotube (on top) that displays pores and, in some parts, consists of a few-layer graphene sheet. The inset shows the FFT of a section that is a crystalline single sheet, as revealed by the hexagonal pattern in the FFT (inset). We also observed few-layered graphene sheets (attached to the tubes) after the unzipping process (Figure 2f). The inset shows the FFT of the square section (indicated with dotted line). The bright spots demonstrate that there are still some crystalline domains after oxidation, whereas the multiple spots indicate the presence of a few stacked graphene layers.

The extent of surface oxidation of all samples was analyzed by XPS. Figure 3a,b displays the change in the N 1s and C 1s core-level spectra, respectively, as a function of the reaction temperature and consequently oxidation degree. Figure 3a shows the N 1s core-level of pristine CNx-MWCNTs with three signals ascribed to molecular nitrogen, substitutional, and pyridine-like nitrogen, at *ca.* 404.0, 400.0, and 397.5 eV, respectively. After oxidation, the intensity of the N₂ and the pyridine-type nitrogen signals decreased, even when mild oxidation took place. For the N₂ signal, the

unzipping process creates defects that most likely allow the release of trapped gaseous nitrogen,³⁵ whereas pyridine-like nitrogen disappears due to preferential oxidation because of its high reactivity.²⁹ Oxidation at temperatures between 60 and 80 °C shifts the N 1s peak to *ca.* 401 eV, suggesting the formation of terminal $-\text{NH}_3^+$ and/or amide (CO-NH) groups.

The XPS data for the ox-N-GNRs, shown in Figure 3b, indicate that oxidizing reactions carried out at 40 and 20 °C result in oxidized GNRs exhibiting moderate oxidation, with the formation of C=O and COOH functional groups, which most likely are located at the edges of graphene nanoribbons domains (see deconvolution of C 1s peaks in Supporting Information Figure S3). In contrast, in ox-N-GNRs prepared at 60 and 80 °C, the C 1s peak due to sp^2 -hybridized carbon atoms (at *ca.* 284.5 eV) broadens considerably due to the formation of sp^3 -hybridized carbon atoms and the resulting C 1s spectra, which is similar to that displayed by graphite oxide^{36–38} and unzipped pure carbon MWCNTs.^{16,17} Nevertheless, the top spectrum in Figure 3b shows the C 1s peak of ox-GNR prepared from pure carbon MWCNTs, and both the C 1s peak shape and the C/O ratio of this sample indicate that its degree of oxidation is much lower when compared to ox-N-GNRs prepared at the same temperature. In order to correlate the oxidation extent with the nanoribbon morphology, the samples prepared at 60 °C with limited amount of oxidizer were also evaluated by XPS, and the results are shown in Figure 3d. In this case, the C 1s peak shape resembles that of samples oxidized at lower temperatures. These results confirm that the oxidation extent can be controlled either by using a lower temperature or by limiting the amount of oxidizer (see deconvoluted peaks in Figure S2, Supporting Information).

After we found that the oxidation extent can be easily controlled by the temperature, we studied the effect of temperature by performing oxidation kinetics at 80 and 20 °C (runs 1 and 4). Figure 4a,b compares the C 1s peak evolution during the first two hours and first hour of the CNx-MWCNT oxidations carried out at 20 and 80 °C, respectively. When the reaction occurred at 20 °C, the oxidation is steady with a gradual change in the peak shape (Figure 4a), whereas the reaction carried out at 80 °C shows a drastic change in the C 1s peak, with significant broadening of the 284.5 eV peak after only 30 min (Figure 4a). Indeed, the semi-quantitative chemical analysis indicates that at 80 °C the carbon content decreased rapidly to 70 atom % after just 15 min, whereas at low temperature, the oxidations proceeded slowly, reaching a similar carbon content (72 atom %) after 2 h (Figure 4c). The strong dependence of oxidation rate upon temperature could be deduced by comparing the peak shape change over time. For example, after 1 min at 80 °C, the C 1s peak shape is similar to that observed after 60 min at 20 °C,

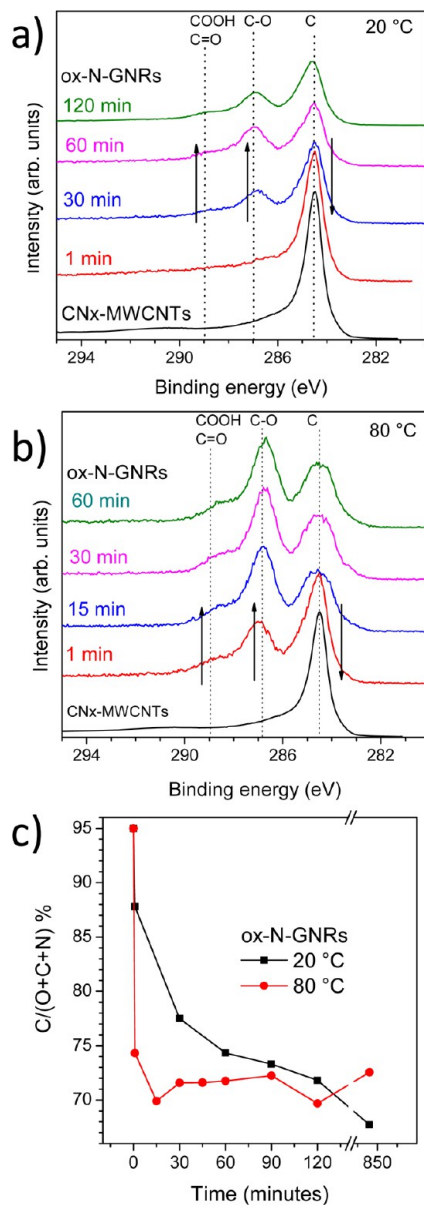


Figure 4. X-ray photoelectron study of the evolution of the carbon, oxygen, and nitrogen content as a function of oxidation extent. Evolution of the C 1s core-level spectra of samples oxidized at (a) 20 °C and (b) 80 °C. (c) Semiquantitative carbon content analysis ($\text{C}/(\text{C} + \text{O} + \text{N})$) of samples shown in (a) and (b). Note that samples were oxidized as long as 14 h (840 min), and the x axis in (c) has a break between 120 and 850 min. In order to observe peaks changes, spectra from the first two hours and the first hour are included for reactions carried out at 80 and 20 °C, respectively.

thus suggesting that the oxidation rate is approximately 60 times higher at 80 °C as compared to that occurring at 20 °C. Regardless of the strong dependence of the oxidation rate with temperature, the C and O content barely changed between 2 and 14 h, which indicates that the oxidized nitrogen-doped graphitic lattice reached equilibrium with the oxidizer medium.

One of the most important differences of these N-doped nanoribbons, when compared to previously

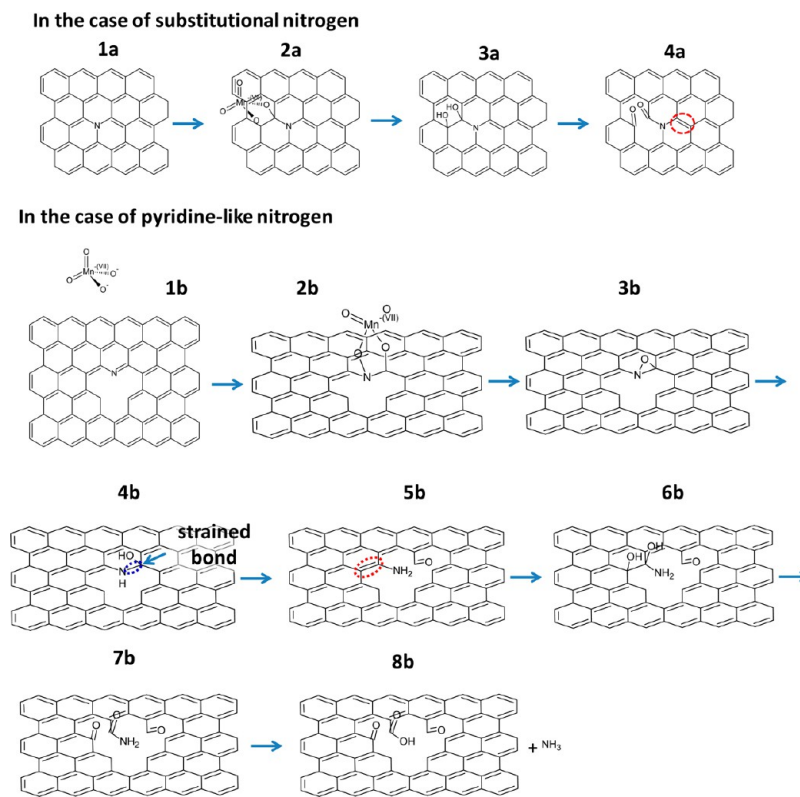


Figure 5. Proposed mechanism for the nanotube oxidation involving the oxidation of pyridine-like and substitutional-like nitrogen atoms within the graphitic lattice of CNx-MWCNTs. All reaction steps are carried out in concentrated H_2SO_4 with an excess of KMnO_4 .

reported nanoribbons prepared by unzipping of pure MWCNTs, is the presence of nitrogen atoms. Figure 3a,b indicates the nitrogen atomic percent of the samples oxidized at different temperatures or with different oxidizer concentration, respectively. The nitrogen content was higher in pristine CNx-MWCNTs with 1.55 atom %, and it decreased as the oxidation degree (C/O atomic ratio) increased, promoted by either temperature or the amount of oxidizer. This clearly indicates that the N atoms are preferential sites for initiating oxidation, and consequently, its content decreases as oxidation increases. Indeed, it has been known that primary and secondary amines could be degraded by oxidation with permanganate to aldehydes and ketones, thus losing nitrogen atoms with the generation of gaseous ammonia.³⁹

All samples were also studied by FTIR spectroscopy (see Figure S4, Supporting Information) in order to identify the functional groups produced by the oxidation process. The ox-N-GNRs prepared at 80 °C (run 4) were compared with graphite oxide (GO) (run 9) prepared by a slight modification of the method reported by Marcano *et al.*³⁸ and with oxidized GNRs prepared using (pure carbon) MWCNTs (ox-GNRs, run 7) and highly crystalline MWCNTs (ox-HC-GNRs, run 8). All samples exhibited the same FTIR peaks identified in graphite oxide.³⁶ The broad band around 3410 cm^{-1} is due to O—H stretching mode, indicating the presence

of water and hydroxyl groups. The peak located at *ca.* 1732 cm^{-1} corresponds to the stretching mode of carboxyl groups, while the peak at 1625 cm^{-1} has been recently found to correspond to water.³⁶ The peaks at *ca.* 1410, 1225, and 1055 cm^{-1} are related to several C—C and C—O vibration modes. The main difference of these spectra, however, is the stronger intensity of the peak located at *ca.* 1732 cm^{-1} , which is due to a comparatively larger number of carbonyl groups in the oxidized N-GNRs. During graphite oxidation, it is well-known that carboxyl groups are formed primarily on the edge of the graphitic sheets.⁴⁰ Thus, the larger number of defects usually contained in CNx-MWCNTs, such as vacancies, and the nitrogen groups located on the walls, are likely to promote the formation of carbonyl groups during oxidation.

The functionalization of the graphitic layers of the CNx-MWCNTs results in expansion, as indicated by the XRD pattern revealing the formation of a broad (001) peak in ox-N-GNRs with a *d* spacing of 0.84 nm (see Supporting Information Figure S5). These phenomena resemble the oxidation of graphite, but unlike the sharp 001 peak shown by GO, the ox-GNR peak is very broad, due to increased disorder and variable spacing of the layers.

Mechanism of Oxidation of CNx Nanotubes. From the characterization described above, it is clear that the oxidation of CNx-MWCNTs is higher when compared to

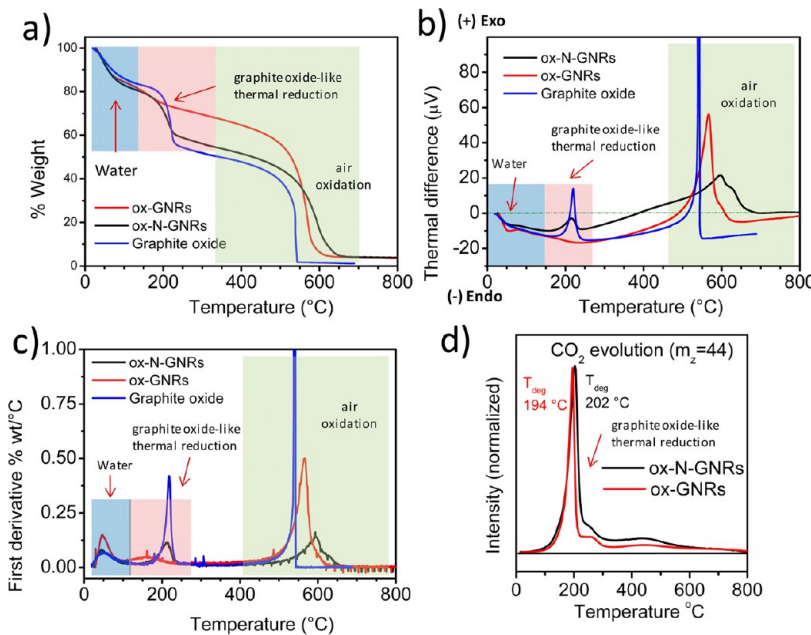


Figure 6. Comparative thermal analysis of oxidized graphene nanoribbons prepared from pure carbon and from nitrogen-doped MWCNTs: (a) TGA analysis of the ox-N-GNRs, ox-GNRs, and graphite oxide in air; corresponding (b) differential thermal analysis (DTA) and (c) first derivative obtained during the TGA scan. (d) Evolution of carbon dioxide by TGA-MS under inert (He) atmosphere. Both curves have been normalized to the peak intensity during the exothermal deoxygenation around 200 °C.

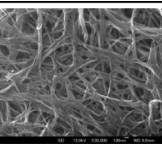
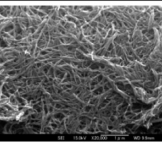
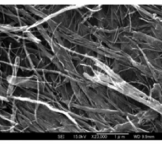
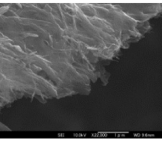
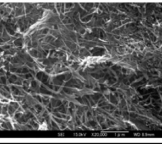
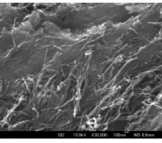
pure carbon MWCNTs. We therefore propose a possible oxidation mechanism (Figure 5). When CN_x-MWCNTs are in contact with the permanganate ion in the sulfuric acid solution, the oxidation of the pure carbon lattice follows the pathway described by Sun *et al.*,⁴¹ in which the oxidation disrupts the hexagonal symmetry of the tubular lattice, thus creating higher order rings that eventually unzip the nanotube. Theoretical calculations have shown that nitrogen-doped carbon favors the formation of vacancies and higher order rings. In addition, nitrogen atoms, either pyridinic or substitutional, exhibit a high charge density,⁴² and consequently, the permanganate ion is strongly attracted to these sites. For substitutional nitrogen, the neighboring carbon atoms oxidize as indicated in Figure 5, 2a–3a. The resulting structure could be further oxidized (Figure 5, 4a), but the nitrogen atom is still relatively stable within the hexagonal lattice. On the other hand, pyridine-like nitrogen atoms are prone to be removed from the structure, as supported by the XPS (see Figure 3a,c). Unlike substitutional nitrogen, the pyridine-like nitrogen is bonded to two (not three) carbon atoms. After reacting with permanganate, the pyridinic C=N bond is oxidized into a highly strained C–O–N bond (Figure 5, 3b–4b). This functional group is further cleaved, and then the pyridine-like nitrogen is transformed into a terminal NH₂ group, which, after further hydrolysis, is removed from the surface of the nanotube as NH₃ leaving a carboxyl group at the edge. The oxidation of the pyridine-like group results in the formation of three C=O groups observed in Figure 5,

8b, which might be partially responsible for the strong carbonyl signal observed by FTIR (Figure S4) in the ox-N-GNR sample.

The higher extent of oxidation was also confirmed by TGA-DTA and TGA-MS comparative experiments of ox-N-GNRs (run 4), ox-GNRs (run 7), and GO (run 9), as shown in Figure 6. The first weight loss below 100 °C displayed in all samples corresponds to water evaporation. This is an endothermic process as indicated by the differential thermal analysis. Then, both ox-N-GNRs and ox-GNRs displayed an exothermic graphite oxide-like deoxygenation when heated around 200 °C. The magnitude of this reaction, as revealed by the weight loss (Figure 6a and more clearly seen in its derivative in Figure 6c) and the exothermic signal (Figure 6b), was higher for ox-N-GNRs than for ox-GNRs. This is in part the result of a larger amount of oxygen groups confirmed by the C/O ratio (see Table 1). When an oxidized carbon sample is heated, most of the oxygen from functional groups is released as CO₂, thus we carried out TGA-MS to study the comparative evolution of this gas in both ox-N-GNRs and ox-GNRs (Figure 6d). As expected, the CO₂ evolution peak in ox-N-GNRs is not only broader, suggesting a greater diversity of functional groups, but also of higher intensity up to 600 °C.

Reduction of Oxidized CN_x Nanotubes. Oxidized GNRs could be reduced to graphene nanoribbons by chemical or thermal methods.^{17,43} We studied comparatively the reduction of ox-N-GNRs (run 4) and two samples of oxidized nanoribbons obtained from two different

TABLE 2. Summary of Reaction Conditions for Reduction Treatments and Results

Run	Type of material	Temp	SEM	XPS data				Observations
				Peak	Position	at. %	C/O	
10	N-GNRs-red300	1 h 300 °C (Ar)		C 1s	284.448	93.48		Stacked ribbons. Moderate reduction. Moderate nitrogen content.
11	N-GNRs-red800	1 h 800 °C (Ar)		C 1s	284.35	95.01		Small ribbons and nanotubes. Structural damage. Highly reduced. Low nitrogen content.
12	GNRs-red800	1 h 800 °C (Ar)		C 1s	284.35	96.32		Mixture of stacked and exfoliated ribbons. Highly reduced
13	HC-GNR-red400	1 h 400°C (Ar)		C 1s	284.5	94.25		Exfoliated ribbons. Assembled into sheets. Moderate reduction.
14	N-GNRs-redNH ₂	3h 85°C NH ₄ OH 0.1M NH ₂ NH ₂ (1% vol)		C 1s	284.477	88.39		Mainly stacked ribbons. Moderate reduction. High nitrogen content.
15	GNRs-redNH ₂	3h 85°C NH ₄ OH 0.1M NH ₂ NH ₂ (1% vol)		C 1s	284.44	91.67		Exfoliated ribbons Assembled into sheets. Highly reduced. High nitrogen content.

pure carbon MWCNTs, ox-GNRs (run 7) and ox-HC-GNRs (run 8). Both thermal and chemical reduction methods were used for the samples, and the results are summarized in Table 2.

For comparison, GNRs prepared by oxidation of MWCNTs based on previous reports¹⁶ and reduced thermally at 800 °C are shown in Figure 7a (TEM image shown in Supporting Information, Figure S6a, whereas the TEM image of the ox-N-GNRs prior to reduction is shown in Figure S6b). SEM images of the nitrogen-doped GNRs reduced at 300 °C (N-GNRs-red300, run 10) and at 800 °C (N-GNRs-red800, run 11) are shown in Figure 7b,c, respectively, whereas the N-GNRs reduced using hydrazine (N-GNRs-redNH₂, run 14) are displayed in Figure 7d. N-GNRs reduced at low temperature (300 °C) (Figure 7b) showed a morphology consisting of ribbons (see also the TEM images in Supporting Information Figure S6c), but unlike GNRs obtained from pure carbon MWCNTs, the structure of N-GNRs was unstable when the heat treatment was carried out at 800 °C (run 11, Figure 7c, and TEM image

in Supporting Information Figure S6d). The resulting structures consist of very small short tubes, ribbons (less than 500 nm long), and carbon nanoparticles. The reason for such a drastic change in morphology during thermal reduction might be due to the higher amount of oxygen groups within the carbon lattice. Chemical reduction using hydrazine also yielded N-GNRs (run 14, N-GNRs-redNH₂), with small diameters (Figure 7d) that contain a considerable amount of carbon nanoparticles (Figure 6d). Due to their reduced dimensions (see inset for size distribution), these structures might have potential applications as catalyst support and electrochemical capacitors due to their higher surface area, as compared to pristine CN_x-MWCNTs. We believe that the structural instability of oxidized nitrogen-doped GNRs results from its chemical reactivity, caused by the presence of a larger number of defects and oxygen groups as compared to oxidized undoped GNRs. However, HRTEM images of samples reduced at 800 °C show some nitrogen-doped graphene sheets, such as the bilayer graphene anchored to a small diameter

nanotube (Figure 7e), and in spite of the large number of defects, after heat treatment, most of the layered structures recovered the hexagonal lattice characteristic of graphene (as seen by the FFT in the inset of Figure 7f).

The reduced samples were also analyzed by Raman and UV–visible spectroscopy, and the results are shown in Supporting Information Figure S7a,b, respectively. In particular, the I_D/I_G intensity ratio, I_G peak position, and the $\pi-\pi^*$ peak position are indicated in the Supporting Information (see Table S1). The shift of the $\pi-\pi^*$ peak position is an indication of the extent of conjugation. We can observe that pristine nitrogen-doped nanotubes (CNx-MWCNTs) show this peak at 275 nm, but after oxidation and the formation of carbon sp^3 domains, it is shifted to 244 nm for ox-N-GNRs (C/O = 2.16) whereas ox-GNR (C/O = 3.12) shows its peak at 236 nm. It is clear that, in spite of being more functionalized, these functional groups are probably not evenly distributed within ox-N-GNRs and some “islands” with sp^2 conjugation remain. Chemical reduction with hydrazine shifts the $\pi-\pi^*$ peak position to 263 nm for N-GNRs-NH₂ (C/O = 10.1), whereas the GNRs after hydrazine reduction shift to a higher wavelength of 268 nm (C/O = 23.3). Both the UV–vis spectra and XPS indicate that pure carbon ox-GNRs are more easily reduced by hydrazine. Therefore, nitrogen atoms not only avoid the homogeneous oxidation but also slow the reduction process in ox-N-GNRs, thus inhibiting the formation of sp^2 -conjugated domains within N-GNRs. Raman results (Figure 7b) are consistent with UV–vis; the G-band position in pristine CNx nanotubes appears at 1585 cm⁻¹, and after oxidation and the formation of sp^3 carbon domains, the G peak shifts to 1600 cm⁻¹. Following the chemical reduction with hydrazine, the position of this peak is shifted back to 1590 cm⁻¹ for N-GNRs and to 1587 cm⁻¹ in the case of pure carbon GNRs. Thermal reduction of ox-N-GNRs at 800 °C also shifts the G band further to 1587 cm⁻¹, which is very close to the original position in pristine CNx-MWCNTs. The presence of remnant oxidized domains in the N-GNR sample reduced at 300 °C is also revealed by the position of the G band, which appears shifted at 1592 cm⁻¹ after reduction.

Finally, the C 1s core-level spectra and the thermal stability of reduced samples are shown in Figure 8a,b and show perfect correlation between the reduction extent (C/O ratio) and thermal stability analyzed by thermogravimetry. CNx-MWCNTs display the typical shape characteristic of sp^2 -hybridized carbon (284.5 eV), and its C/O ratio is very high as expected from CVD-synthesized carbon. GNRs from pure carbon MWCNTs obtained by thermal reduction at 800 °C (GNRs-red800) show a C 1s peak very similar to the pristine CNx-MWCNT material, indicating the complete loss of oxygen functional groups and recovery of the sp^2 hybridization and a high C/O ratio of 26.2. On the other

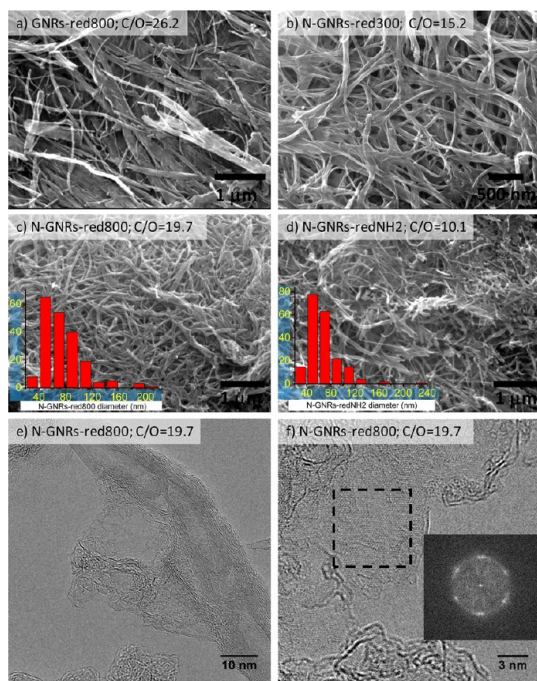


Figure 7. Images showing the morphologies of oxidized GNRs after the thermal or chemical reduction with hydrazine. (a) SEM image of GNRs obtained from pure carbon MWCNTs thermally reduced at 800 °C (run 12). (b) SEM image of N-containing GNRs thermally reduced at 300 °C (run 10). (c) SEM image of N-containing GNRs thermally reduced at 800 °C (run 11). (d) SEM image of chemically reduced N-GNRs using hydrazine (run 14). (e,f) HRTEM images of N-GNRs thermally reduced at 800 °C (run 11). The insets in (c,d) show the corresponding diameter distributions, and the inset shown in (f) corresponds to the FFT of the area indicated in dotted square.

hand, N-doped GNRs reduced by the same process (N-GNRs-red800) show a small peak located at 289 eV in addition to the main peak at 284.5 eV, which is due to residual carboxyl groups and defects, which decrease the C/O ratio to 19.7. In addition, the peak located at 284.5 eV is broader, suggesting the presence of carbon atoms exhibiting sp^3 hybridization and C–N and C–O bonds. The thermal stability of these three highly reduced samples is similar, but it decreases slightly as the reduction extent increases (C/O ratio).

In addition, carboxyl defects are evident in the N-GNR sample reduced at 300 °C (N-GNRs-red300), in which a peak located at 288.7 eV and a shoulder located at *ca.* 286.2 eV caused by C–O groups are observed. The C/O ratio of this sample is lower (15.2), and its thermal stability decreases considerably. Indeed, a weight loss could be observed at 250 °C, due to the loss of oxygen functional groups. Similarly, the hydrazine-reduced sample shows the contribution of C–N or C–O groups close to 286.2 eV, but the carboxyl groups were successfully eliminated. Potential applications of reduced nitrogen-doped GNRs include electrochemical energy storage and electrochemical biosensors. Figure S8a,b shows the cyclic voltammetry behavior for the GNRs prepared by thermal reduction

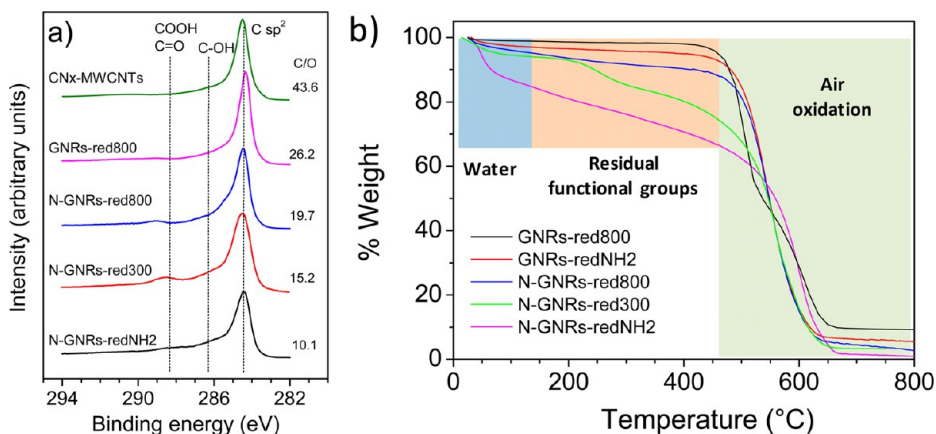


Figure 8. (a) XPS C 1s core-level spectra of GNR samples after thermal or chemical reduction. From top to bottom: pristine CNx-MWCNTs as reference, GNRs obtained by oxidation of MWCNTs followed by thermal reduction at 800 °C (GNRs-red800), N-GNRs obtained by oxidation of CNx-MWCNTs and thermal reduction at 800 °C (N-GNRs-red800), and by thermal reduction at 300 °C from oxidized (N-GNRs-red300) and from chemical reduction using hydrazine (N-GNRs-redNH2). The presence of oxygenated groups as defects is confirmed by thermogravimetric analysis in (b), where the thermal stability matches the sequence of the reduction extent (C/O ratio) measured by XPS.

and nitrogen-doped GNRs obtained by reduction with hydrazine, respectively. Both samples show the typical shape of a double-layer charging (capacitive current) with a broad peak around 0.4 V (vs Ag/AgCl) most likely due to residual functional groups. Nevertheless, in spite of the small size, the capacitance shows a moderate value of *ca.* 50 F/g for both samples, twice of that reported for pristine MWCNTs. Further activation of the nanoribbons is proposed in order to reach higher capacitance values.

CONCLUSIONS

N-GNRs could be synthesized by oxidative unzipping of CNx-MWCNTs using KMnO₄ in H₂SO₄/H₃PO₄ mixture. We proposed the structural evolution from longitudinally unzipped nanotubes to “stiff” nanoribbons and finally “soft” (highly oxidized) nanoribbons. The degree of functionalization of the ox-N-GNRs is higher than that of pure carbon ox-GNRs prepared under the same reaction conditions, as confirmed by XPS, TGA, FTIR, and TGA-MS. This is due to the high

chemical reactivity of nitrogen-doped MWCNTs. Unzipping of CNx-MWCNTs with diameters smaller than 30 nm did not occur, although these structures were oxidized. The oxidation process decreases the concentration of nitrogen groups on the surface of GNRs and could be used as a method to control nitrogen concentration within the nanoribbons. For instance, by controlling the degree of oxidation, the N atomic % could be reduced from 1.56% in pristine CNx-MWCNTs down to 0.31 atom % in nitrogen-doped oxidized graphene nanoribbons. The thermal reduction at relatively low temperature (300 °C) results in graphene nanoribbons with 0.37 atom % of nitrogen. After the thermal reduction at 800 °C, the hexagonal carbon lattice could be restored. The chemical reduction with hydrazine results in nitrogen-doped nanoribbons with low thermal resistance but high nitrogen content. A reaction mechanism of the oxidation of nitrogen functional groups in CNx-MWCNTs was proposed. This work provides further insight in the unzipping mechanism of different types of MWCNTs.

EXPERIMENTAL SECTION

Materials. Sulfuric acid (H₂SO₄, 95 wt %), hydrochloric acid (HCl, 36–37% wt), potassium permanganate (KMnO₄, 99%), phosphoric acid (H₃PO₄, 85 wt %), ferrocene (Cp₂Fe), hydrogen peroxide (H₂O₂, 30 wt %), benzylamine (C₇H₉N), and synthetic graphite (400 mesh) were purchased from Wako Chemicals. Hydrazine hydrate (N₂H₄·H₂O, hydrazine 65 wt %) was purchased from Sigma-Aldrich. Synthetic graphite was acquired from Wako, Japan.

Carbon Nanotube Synthesis. MWCNTs were synthesized by spray-assisted CVD, using Ar as carrier gas; the material was then collected from the inner wall of a quartz tube as described elsewhere.⁴⁴ CNx-MWCNTs were synthesized using a 6 wt % solution of ferrocene, used as catalyst, and benzylamine as a carbon/nitrogen source. In a typical procedure, the ferrocene/benzylamine solution was nebulized and carried out by an Ar flow rate (2.5 L/min) through a quartz tube heated at 850 °C.

Chemical Oxidation and Unzipping of CNx-MWCNT. CNx-MWCNTs were unzipped by oxidation using a method similar to that reported by Higginbotham *et al.*¹⁶ Typically, 800 mg of CNx was sonicated for 1 h in 100 mL of H₂SO₄. Later, 20 mL of H₃PO₄ was added, and the mixture was stirred on a hot plate set at 80 °C. Subsequently, 4.0 g of KMnO₄ was slowly added, and the reaction mixture was left to react for 2.0 h (Caution: permanganic acid oxidations are potentially explosive and should be carried out inside a fume hood with a safety shield protector). After this time, the reaction mixture was slowly poured into a stirred solution of 10 mL of H₂O₂ in 400 mL of cold water. The sample was centrifuged and washed with diluted HCl and H₂SO₄ solutions and, finally, three times with distilled water. After freeze-drying, 679.0 mg of oxidized N-GNRs (ox-N-GNRs) was obtained. A series of reactions were carried out in order to study the effect of temperature and oxidizer concentration. Typically, 200 mg of CNx-MWCNTs was dispersed ultrasonically

(1 h) in a mixture of 50 mL of H_2SO_4 and 10 mL of H_3PO_4 . To study the effect of oxidizer, the hot plate temperature was fixed to 60 °C and the mass ratio of oxidizer to CNx-MWCNTs was varied in three concentrations: 1:1, 2.5:1, and 5:1. When studying the effect of temperature, the mass ratio of the oxidizer to CNx-MWCNTs was fixed to 5:1, and the hot plate temperatures were varied (20, 40, 60, and 80 °C, runs 1, 2, 3, and 4, respectively). Finally, when studying the effect of reaction times, samples were left reacting for different periods of time, ranging from 1 min to 14 h, and the oxidation was stopped by pouring the reacting suspensions in an aqueous solution of H_2O_2 . All samples were neutralized with an excess of H_2O_2 and were washed with diluted H_2SO_4 , HCl, and finally three times distilled H_2O , followed by freeze-drying. For comparison, MWCNTs and highly crystalline MWCNTs also prepared by CVD according to Botello-Mendez *et al.*⁴⁵ were also unzipped using the same method explained above; samples were labeled ox-GNRs and ox-HC-GNRs (runs 7 and 8), respectively. Samples were also purified in the same way as that described for the ox-N-GNR samples. For comparison purposes, graphite oxide was oxidized (run 9) using a slight modification of the improved method described by Marcano *et al.*³⁸ Typically, 1 g of graphite and 5 g of $KMnO_4$ were added to 50 mL of H_2SO_4 and 10 mL of H_3PO_4 and heated to 40 °C. The reaction mixtures turn into thick slurry and after 2 h are poured in 500 mL of a mixture of ice and water with 5 mL of hydrogen peroxide. The GO was purified by centrifugation and washing and finally freeze-dried similarly to ox-N-GNRs.

Hydrazine Reduction. Fifty milligrams of oxidized nanoribbons (ox-N-GNRs or ox-GNRs) was added to 100 mL of ammonia solution (NH_4OH , 0.1 N) to give a dark brown dispersion. Later, 1 mL of $N_2H_4 \cdot H_2O$ (65.0 wt %) was added, and the mixture was heated to 85 °C for 3 h. The gradual darkening of the mixture and flocculation of the dispersed nanoribbons indicate that chemical reduction took place. The hydrazine-reduced nitrogen-doped GNRs (N-GNRs-redNH₂) and the hydrazine-reduced GNRs (GNRs-NH₂) were purified by centrifugation/redisersion in distilled water followed by freeze-drying.

Thermal Reduction. ox-N-GNRs and ox-GNRs were deposited on a ceramic crucible and heated in a tubular furnace. The temperature was increased over a 20 min period from room temperature to 800 °C under a dry Ar flow. After 1 h, the furnace was cooled and the sample was removed and stored for analysis (N-GNRs-red800 and GNRs-red800). In one experiment, we used abrupt heating at relatively low temperature by introducing the sample in a preheated furnace at 300 °C, using the same flow conditions and time as described above (N-GNRs-red300).

Characterization. The overall morphology of the samples was studied by SEM (JEOL JSM-6335 operating at 15–20 kV). High-resolution transmission electron microscopy (HRTEM) was carried out in a JEOL JEM-2100F, operating at 80 kV and equipped with a CEOS Double Cs. Thermogravimetric/differential thermal analysis (TGA/DTA) was carried out on TGA 8120 equipment under air flow (300 mL/min) and a 10 K/min heating rate using alumina powder as reference. Thermogravimetric analysis coupled with mass spectroscopy (TGA-MS) was carried out using a He/O_2 80/20 flow in a Rigaku ThermoMass Photo equipment. X-ray photoelectron spectroscopy (XPS) analysis was carried out using the Al $K\alpha$ line in an Axis-Ultra, Kratos, UK. The XPS analysis chamber was operated at 10^{-9} Torr, a 700 $\mu m \times 300 \mu m$ area was studied, and the analyzer was set at 20 eV pass energy. Samples were grounded, and an electron gun was used to avoid charging during the measurements. Samples were referenced to the C 1s sp^2 peak at 284.5 eV. Semiquantitative elemental analysis was carried out using the C 1s, O 1s, and N 1s peaks from XPS, with relative sensitivity factors of (1, 2.93, and 1.8, respectively). Raman spectroscopy was carried out in a Renishaw Micro Raman using the 785 and 633 nm lines. Fourier transformed infrared (FTIR) spectroscopic studies were carried out on Nicolet 6700 equipment. GNR samples (oxidized and reduced) were ground with KBr and were pressed into pellets for analyses in transmittance mode. X-ray diffraction patterns were obtained using a PANalytical Xpert Pro equipment using the Cu $K\alpha$ line. UV-vis spectra were obtained after sonication of a 1 mg/mL sample in deionized water. The water-dispersed material was allowed to sediment, and then 200 μL of the dispersion was

quickly mixed by inversion with 3.0 mL of deionized water and measured immediately.

Conflict of Interest: The authors declare no competing financial interest.

Acknowledgment. M.T., R.C.-S., S.V.-D., F.T.-L., and M.E. acknowledge support from the Research Center for Exotic Nanocarbons, Japan, regional Innovation Strategy Program by the Excellence, JST. M.T. also acknowledges support from the Penn State Center for Nanoscale Science for seed grant on defects in 2-D Layered Materials (DMR-0820404).

Supporting Information Available: SEM images, diameter distribution, XPS wide scan spectrum, and thermogravimetric analysis of pristine CNx-MWCNTs; SEM images depicting the morphologies of the oxidized nitrogen-doped graphene nanoribbons (ox-N-GNRs) prepared at 60 °C using a lower oxidizer to nanotube ratio; deconvoluted C 1s core-level spectra of ox-N-GNRs at different temperatures; Fourier transformed infrared spectroscopy spectra of different types of oxidized GNRs compared to graphite oxide; XRD patterns of pristine nitrogen-doped MWCNTs, oxidized N-doped GNRs, and thermally reduced GNRs; TEM images of oxidized GNRs, N-doped GNRs, and thermally reduced N-doped GNRs; Raman and UV-vis spectra of samples; spectroscopic data from Raman and UV-vis of samples; and cyclic voltammetry curves of hydrazine-reduced GNRs and N-doped GNRs. This material is available free of charge via the Internet at <http://pubs.acs.org>.

REFERENCES AND NOTES

- Novoselov, K. S.; Geim, A. K.; Morozov, S. V.; Jiang, D.; Zhang, Y.; Dubonos, S. V.; Grigorieva, I. V.; Firsov, A. A. Electric Field Effect in Atomically Thin Carbon Films. *Science* **2004**, *306*, 666–669.
- Fujita, M.; Wakabayashi, K.; Nakada, K.; Kusakabe, K. Peculiar Localized State at Zigzag Graphite Edge. *J. Phys. Soc. Jpn.* **1996**, *65*, 1920–1923.
- Terrones, M.; Botello-Mendez, A. R.; Campos-Delgado, J.; Lopez-Urias, F.; Vega-Cantu, Y. I.; Rodriguez-Macias, F. J.; Elias, A. L.; Munoz-Sandoval, E.; Cano-Marquez, A. G.; Charlher, J. C.; *et al.* Graphene and Graphite Nanoribbons: Morphology, Properties, Synthesis, Defects and Applications. *Nano Today* **2010**, *5*, 351–372.
- Rafiee, M. A.; Lu, W.; Thomas, A. V.; Zandiatashbar, A.; Rafiee, J.; Tour, J. M.; Koratkar, N. A. Graphene Nanoribbon Composites. *ACS Nano* **2010**, *4*, 7415–7420.
- Asai, M.; Ohba, T.; Iwanaga, T.; Kanoh, H.; Endo, M.; Campos-Delgado, J.; Terrones, M.; Nakai, K.; Kaneko, K. Marked Adsorption Irreversibility of Graphitic Nanoribbons for CO_2 and H_2O . *J. Am. Chem. Soc.* **2011**, *133*, 14880–14883.
- Landis, E. C.; Klein, K. L.; Liao, A.; Pop, E.; Hensley, D. K.; Melechko, A. V.; Hamers, R. J. Covalent Functionalization and Electron-Transfer Properties of Vertically Aligned Carbon Nanofibers: The Importance of Edge-Plane Sites. *Chem. Mater.* **2010**, *22*, 2357–2366.
- Campos-Delgado, J.; Romo-Herrera, J. M.; Jia, X.; Cullen, D. A.; Muramatsu, H.; Kim, Y. A.; Hayashi, T.; Ren, Z.; Smith, D. J.; Okuno, Y.; *et al.* Bulk Production of a New Form of sp^2 Carbon: Crystalline Graphene Nanoribbons. *Nano Lett.* **2008**, *8*, 2773–2778.
- Yang, X.; Dou, X.; Rouhanipour, A.; Zhi, L.; Raeder, H. J.; Mullen, K. Two-Dimensional Graphene Nanoribbons. *J. Am. Chem. Soc.* **2008**, *130*, 4216–4217.
- Terrones, M. Materials Science: Nanotubes Unzipped. *Nature* **2009**, *458*, 845–846.
- Jiao, L.; Zhang, L.; Wang, X.; Diankov, G.; Dai, H. Narrow Graphene Nanoribbons from Carbon Nanotubes. *Nature* **2009**, *458*, 877–880.
- Laura Elias, A.; Botello-Mendez, A. R.; Meneses-Rodriguez, D.; Jehova Gonzalez, V.; Ramirez-Gonzalez, D.; Ci, L.; Munoz-Sandoval, E.; Ajayan, P. M.; Terrones, H.; Terrones, M. Longitudinal Cutting of Pure and Doped Carbon Nanotubes To Form Graphitic Nanoribbons Using Metal Clusters as Nanoscalpels. *Nano Lett.* **2010**, *10*, 366–372.

12. Cano-Marquez, A. G.; Rodriguez-Macias, F. J.; Campos-Delgado, J.; Espinosa-Gonzalez, C. G.; Tristan-Lopez, F.; Ramirez-Gonzalez, D.; Cullen, D. A.; Smith, D. J.; Terrones, M.; Vega-Cantu, Y. I. Ex-MWCNT: Graphene Sheets and Ribbons Produced by Lithium Intercalation and Exfoliation of Carbon Nanotubes. *Nano Lett.* **2009**, *9*, 1527–1533.
13. Kosynkin, D. V.; Lu, W.; Sinitkii, A.; Pera, G.; Sun, Z.; Tour, J. M. Highly Conductive Graphene Nanoribbons by Longitudinal Splitting of Carbon Nanotubes Using Potassium Vapor. *ACS Nano* **2011**, *5*, 968–974.
14. Kim, K.; Sussman, A.; Zettl, A. Graphene Nanoribbons Obtained by Electrically Unwrapping Carbon Nanotubes. *ACS Nano* **2010**, *4*, 1362–1366.
15. Shinde, D. B.; Debgupta, J.; Kushwaha, A.; Aslam, M.; Pillai, V. K. Electrochemical Unzipping of Multi-walled Carbon Nanotubes for Facile Synthesis of High-Quality Graphene Nanoribbons. *J. Am. Chem. Soc.* **2011**, *133*, 4168–4171.
16. Higginbotham, A. L.; Kosynkin, D. V.; Sinitkii, A.; Sun, Z.; Tour, J. M. Lower-Defect Graphene Oxide Nanoribbons from Multiwalled Carbon Nanotubes. *ACS Nano* **2010**, *4*, 2059–2069.
17. Kosynkin, D. V.; Higginbotham, A. L.; Sinitkii, A.; Lomeda, J. R.; Dimiev, A.; Price, B. K.; Tour, J. M. Longitudinal Unzipping of Carbon Nanotubes To Form Graphene Nanoribbons. *Nature* **2009**, *458*, 872–876.
18. Sinitkii, A.; Dimiev, A.; Kosynkin, D. V.; Tour, J. M. Graphene Nanoribbon Devices Produced by Oxidative Unzipping of Carbon Nanotubes. *ACS Nano* **2010**, *4*, 5405–5413.
19. Cataldo, F.; Compagnini, G.; Patane, G.; Ursini, O.; Angelini, G.; Ribic, P. R.; Margaritondo, G.; Cricenti, A.; Palleschi, G.; Valentini, F. Graphene Nanoribbons Produced by the Oxidative Unzipping of Single-Wall Carbon Nanotubes. *Carbon* **2010**, *48*, 2596–2602.
20. Wei, J.; Lv, R.; Guo, N.; Wang, H. G.; Bai, X.; Mathkar, A.; Kang, F. Y.; Zhu, H. W.; Wang, K. L.; Wu, D. H.; et al. Preparation of Highly Oxidized Nitrogen-Doped Carbon Nanotubes. *Nanotechnology* **2012**, *23*, 155601.
21. Terrones, M. Sharpening the Chemical Scissors To Unzip Carbon Nanotubes: Crystalline Graphene Nanoribbons. *ACS Nano* **2010**, *4*, 1775–1781.
22. Lv, R.; Terrones, M. Towards New Graphene Materials: Doped Graphene Sheets and Nanoribbons. *Mater. Lett.* **2012**, *78*, 209–218.
23. Botello-Mendez, A. R.; Cruz-Silva, E.; Lopez-Urias, F.; Sumpter, B. G.; Meunier, V.; Terrones, M.; Terrones, H. Spin Polarized Conductance in Hybrid Graphene Nanoribbons Using 5–7 Defects. *ACS Nano* **2009**, *3*, 3606–3612.
24. Boukhvalov, D. W.; Katsnelson, M. I. Chemical Functionalization of Graphene with Defects. *Nano Lett.* **2008**, *8*, 4373–4379.
25. Zhu, Y.; Higginbotham, A. L.; Tour, J. M. Covalent Functionalization of Surfactant-Wrapped Graphene Nanoribbons. *Chem. Mater.* **2009**, *21*, 5284–5291.
26. Yu, Z.; Hu, M. L.; Zhang, C. X.; He, C. Y.; Sun, L. Z.; Zhong, J. Transport Properties of Hybrid Zigzag Graphene and Boron Nitride Nanoribbons. *J. Phys. Chem. C* **2011**, *115*, 10836–10841.
27. Zheng, X. H.; Wang, X. L.; Abtew, T. A.; Zeng, Z. Building Half-Metallicity in Graphene Nanoribbons by Direct Control over Edge States Occupation. *J. Phys. Chem. C* **2010**, *114*, 4190–4193.
28. Li, Y.; Zhou, Z.; Shen, P.; Chen, Z. Spin Gapless Semiconductor-Metal-Half-Metal Properties in Nitrogen-Doped Zigzag Graphene Nanoribbons. *ACS Nano* **2009**, *3*, 1952–1958.
29. Cruz-Silva, E.; Barnett, Z. M.; Sumpter, B. G.; Meunier, V. Structural, Magnetic, and Transport Properties of Substitutionally Doped Graphene Nanoribbons from First Principles. *Phys. Rev B* **2011**, *83*, 155445.
30. Kim, H.; Lee, K.; Woo, S. I.; Jung, Y. On the Mechanism of Enhanced Oxygen Reduction Reaction in Nitrogen-Doped Graphene Nanoribbons. *Phys. Chem. Chem. Phys.* **2011**, *13*, 17505–17510.
31. Cervantes-Sodi, F.; Csanyi, G.; Piscanec, S.; Ferrari, A. C. Electronic Properties of Chemically Modified Graphene Ribbons. *Phys. Status Solidi B* **2008**, *245*, 2068–2071.
32. Wei, X.-L.; Fang, H.; Wang, R.-Z.; Chen, Y.-P.; Zhong, J.-X. Energy Gaps in Nitrogen Delta-Doping Graphene: A First-Principles Study. *Appl. Phys. Lett.* **2011**, *99*.
33. Yu, S. S.; Zheng, W. T.; Wen, Q. B.; Jiang, Q. First Principle Calculations of the Electronic Properties of Nitrogen-Doped Carbon Nanoribbons with Zigzag Edges. *Carbon* **2008**, *46*, 537–543.
34. Pan, S.; Aksay, I. A. Factors Controlling the Size of Graphene Oxide Sheets Produced via the Graphite Oxide Route. *ACS Nano* **2011**, *5*, 4073–4083.
35. Terrones, M.; Kamalakaran, R.; Seeger, T.; Ruhle, M. Novel Nanoscale Gas Containers: Encapsulation of N₂ in CN_x Nanotubes. *Chem. Commun.* **2000**, *23*, 2335–2336.
36. Dimiev, A. M.; Alemany, L. B.; Tour, J. M. Graphene Oxide. Origin of Acidity, Its Instability in Water, and a New Dynamic Structural Model. *ACS Nano* **2013**, *7*, 576–578.
37. Becerril, H. A.; Mao, J.; Liu, Z.; Stoltberg, R. M.; Bao, Z.; Chen, Y. Evaluation of Solution-Processed Reduced Graphene Oxide Films as Transparent Conductors. *ACS Nano* **2008**, *2*, 463–470.
38. Marcano, D. C.; Kosynkin, D. V.; Berlin, J. M.; Sinitkii, A.; Sun, Z.; Slesarev, A.; Alemany, L. B.; Lu, W.; Tour, J. M. Improved Synthesis of Graphene Oxide. *ACS Nano* **2010**, *4*, 4806–4814.
39. Rawalay, S. S.; Shechter, H. Oxidation of Primary, Secondary, and Tertiary Amines with Neutral Permanganate. A Simple Method for Degrading Amines to Aldehydes and Ketones. *J. Org. Chem.* **1967**, *32*, 3129–3131.
40. Jeong, H. K.; Lee, Y. P.; Lahaye, R.; Park, M. H.; An, K. H.; Kim, I. J.; Yang, C. W.; Park, C. Y.; Ruoff, R. S.; Lee, Y. H. Evidence of Graphitic AB Stacking Order of Graphite Oxides. *J. Am. Chem. Soc.* **2008**, *130*, 1362–1366.
41. Sun, T.; Fabris, S. Mechanisms for Oxidative Unzipping and Cutting of Graphene. *Nano Lett.* **2012**, *12*, 17–21.
42. Cruz-Silva, E.; Lopez-Urias, F.; Munoz-Sandoval, E.; Sumpter, B. G.; Terrones, H.; Charlier, J.-C.; Meunier, V.; Terrones, M. Electronic Transport and Mechanical Properties of Phosphorus- and Phosphorus-Nitrogen-Doped Carbon Nanotubes. *ACS Nano* **2009**, *3*, 1913–1921.
43. Zhu, Y.; Li, X. Y.; Cai, Q. J.; Sun, Z. Z.; Casillas, G.; Jose-Yacaman, M.; Verduzco, R.; Tour, J. M. Quantitative Analysis of Structure and Bandgap Changes in Graphene Oxide Nanoribbons during Thermal Annealing. *J. Am. Chem. Soc.* **2012**, *134*, 11774–11780.
44. Villalpando-Paez, F.; Zarnudio, A.; Elias, A. L.; Son, H.; Barros, E. B.; Chou, S. G.; Kim, Y. A.; Muramatsu, H.; Hayashi, T.; Kong, J.; et al. Synthesis and Characterization of Long Strands of Nitrogen-Doped Single-Walled Carbon Nanotubes. *Chem. Phys. Lett.* **2006**, *424*, 345–352.
45. Botello-Mendez, A.; Campos-Delgado, J.; Morelos-Gomez, A.; Romo-Herrera, J. M.; Rodriguez, A. G.; Navarro, H.; Vidal, M. A.; Terrones, H.; Terrones, M. Controlling the Dimensions, Reactivity and Crystallinity of Multiwalled Carbon Nanotubes Using Low Ethanol Concentrations. *Chem. Phys. Lett.* **2008**, *453*, 55–61.